infrastructures

MDPI

Article

Study on Interannual Variation Characteristics of Thermal and Humid Environments in Metro Tunnels Based on Different Climate Zones in China

Jiangyan Ma [1], Shuang Qiu [2], Lin Huang [1,*], Baoshun Deng [1], Lei He [1], Xiaoling Cao [2] and Qian Zhang [2]

[1] China Railway First Survey and Design Institute Group Co., Ltd., Xi'an 710043, China; jzy_majiangyan.yy@crcc.cn (J.M.); dengbaoshun.yy@crcc.cn (B.D.); jzy_helei.yy@crcc.cn (L.H.)
[2] School of Mechanical Engineering, Southwest Jiaotong University, Chengdu 611756, China; 3361324806@my.swjtu.edu.cn (S.Q.); xlcao@swjtu.edu.cn (X.C.); zq9812@my.swjtu.edu.cn (Q.Z.)
* Correspondence: jzy_huanglin.yy@crcc.cn

Abstract

To systematically investigate the issues of tunnel overheating and excessive humidity, this study integrates theoretical analysis, experimental research, and numerical simulations. It examines the coupled heat and moisture transfer behavior in the surrounding rock of metro tunnels and its impact on the tunnel's thermal and humid environment. Based on the theory of heat and moisture transport in porous media, a coupled mathematical model is developed using relative humidity and temperature gradients as the driving potentials. Taking into account the climatic zoning of China, Beijing, Shanghai, Guangzhou, and Kunming are selected as representative cities for cold, hot summer/cold winter, hot summer/warm winter, and temperate climate regions, respectively. The interannual variation characteristics of the thermal and humidity conditions inside metro tunnels in these cities are analyzed and compared. The results indicate that across different climatic zones, higher outdoor peak air temperatures lead to higher peak air temperatures inside the tunnels. The thickness of the thermal regulation zone is primarily influenced by the initial rock temperature and the annual average atmospheric temperature. The thickness of the moisture regulation zone is affected by both the annual temperature fluctuation and the annual average relative humidity, increasing with greater annual atmospheric temperature variation.

Keywords: surrounding rock thermal–humidity coupling; metro segment tunnel; thermal and humid environment; the temperature regulation zone; the moisture regulation zone

Check for updates

Academic Editor: Giuseppe Loprencipe

Received: 12 December 2025
Revised: 1 February 2026
Accepted: 5 February 2026
Published: 7 February 2026

Copyright: © 2026 by the authors. Licensee MDPI, Basel, Switzerland. This article is an open access article distributed under the terms and conditions of the Creative Commons Attribution (CC BY) license.

1. Introduction

The accelerated pace of urbanization and the accompanying surge in urban population have resulted in a marked imbalance between the supply and demand of surface land. This imbalance has given rise to numerous challenges such as traffic congestion, environmental degradation, and inadequate infrastructure. In this paper, the development of underground spaces has emerged as a viable strategy to mitigate these issues. Underground environments are characterized by stable annual temperature, high thermal inertia, and minimal external disturbance to their thermal and humidity conditions. In China, the development of underground spaces is largely propelled by the construction of underground rail transit systems as a means to alleviate surface traffic congestion [1]. Among these, metro systems represent the predominant form of ongoing underground construction [2]. As a significant

part of underground infrastructure, metro tunnels face critical environmental challenges, notably high humidity levels and residual heat accumulation. Elevated humidity can lead to frequent condensation issues within metro stations, adversely affecting equipment performance and the longevity of facilities [3,4]. Additionally, the heat retention in the surrounding rock over prolonged operation periods can result in tunnel temperature rises, posing potential safety risks to train operation [5,6].

The significant thermal and moisture storage capacity of the surrounding rock in interval tunnels is a major contributor to the high temperature and humidity levels within the tunnel environment [7]. Since the surrounding rock constitutes a porous medium, its internal heat transfer and moisture migration processes are inherently coupled, thereby contributing to the complexity of the tunnel's thermal and humid environment. Current research, both domestically and internationally, on heat and moisture transfer within surrounding rock predominantly focuses on tunnel and roadway contexts, divided into two primary areas: single-phase heat transfer and thermo-humid coupled transfer. In studies of single heat transfer, Zhu et al. [8], using the field-measured data from a domestic coal mine, investigated the cyclic dynamic variations in the thermal regulation zone in severely thermally affected mine drive tunnels and developed a mathematical model for the heat regulation and heat storage in tunnel surrounding rock. Wang et al. [9], through scaled model experiments, simulated the evolution of thermal storage layers around metro tunnel surrounding rock under cyclic dynamic temperature conditions, covering a span of 17 years from initial reinstatement to long-term operation. Their work delineated the distribution of soil temperature over time into dynamic expansion and stabilization phases, revealing the evolution of temperature with depth and the associated heat storage characteristics. Concerning thermo-humid coupling studies in the surrounding rock, Wang and Li et al. [10,11], concerning the high-temperature issues in surrounding rock caused by mine excavation, constructed mathematical models for coupled heat and moisture transfer, validating the models' efficacy. Both studies highlighted that neglecting latent heat effects leads to deviations in temperature predictions within the surrounding rock during modeling. Liu et al. [12] focused on fissured surrounding rock in cold-region tunnels, establishing an anisotropic coupled model based on seepage mechanics and heat transfer theories, incorporating initial fissure features to accurately simulate moisture migration and heat transfer processes within the surrounding rock.

Despite advances in current research, most studies on the temperature and humidity fields within tunnels have overlooked the dynamic coupling effects between surrounding rock and air, focusing solely on individual heat transfer processes. Researchers such as Jiang, Vasilyev G.P., and Sun et al. [13–15] have conducted studies on tunnel heat transfer, establishing relevant thermal models and exploring temperature distribution patterns, yet they generally fail to consider the thermal–humid coupling effects. In physical reality, moisture transfer and heat transfer are bidirectionally coupled; moisture migration accompanied by latent heat release or absorption during phase change significantly influences thermal transmission. Ignoring the thermal–humid coupling inevitably introduces limitations to the study.

Therefore, this study establishes a coupled heat and moisture model of the surrounding rock and air within the tunnel, comprehensively considering thermal transfer and moisture migration processes to more accurately reflect the dynamic interactions of temperature and humidity between the tunnel air and the surrounding rock. Additionally, a 20-year simulation of the heat and moisture conditions inside metro tunnel segments is conducted for typical cities across various climate zones. The study systematically analyzes and compares the interannual variations in air temperature and humidity inside the tunnels, as well as the thermal and moisture characteristics of the surrounding rock in each region. The

purpose of this study is to improve the physical realism and long-term prediction accuracy of tunnel thermal and humid environment simulation, and to provide some relevant references for subway infrastructure operation and maintenance, equipment optimization and life extension.

2. Mathematical–Physical Model

2.1. Physical Model

As illustrated in Figure 1, this study centers on metro interval tunnels. The physical model representing heat and moisture transfer within the tunnel is depicted in Figure 2. The surrounding rock of the tunnel is modeled as a composite structure, consisting of a 0.35-m-thick concrete lining and an adjacent soil layer. Due to temperature differences and vapor pressure gradients between the moist air inside the tunnel and the inner surface of the concrete lining, simultaneous convective heat and mass transfer occur. The concrete lining transmits the absorbed heat and moisture to the outer soil layer through thermal conduction and moisture diffusion. Subsequently, the soil facilitates further heat transfer via thermal conduction and the migration of pore water and water vapor, thereby enabling continuous heat and moisture exchange between the lining and the surrounding geological medium. In Figure 1, "L" indicates the distance from the tunnel exit.

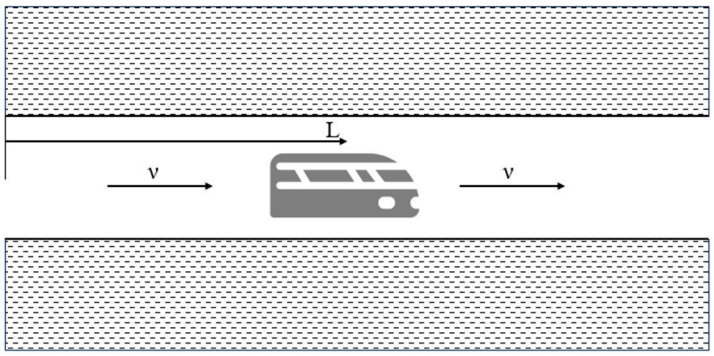


Figure 1. The schematic diagram of the research area of the metro tunnel.

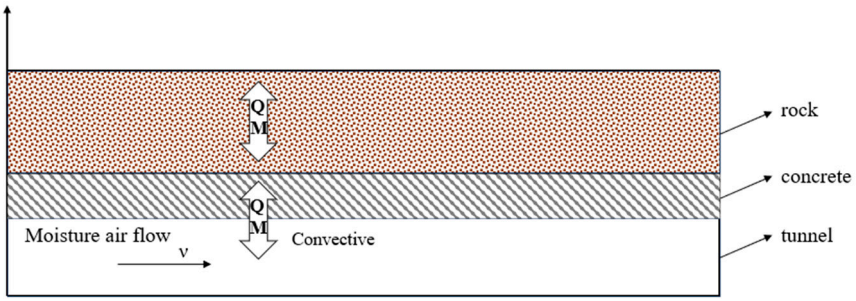


Figure 2. Physical model diagram of heat and moisture transfer in metro tunnel.

2.2. Mathematical Model

The coupled heat and moisture transfer in surrounding rock is a complex process influenced by multiple factors, including the thermophysical and hygric properties of the rock and the internal tunnel environment. To simplify the computational model, the following assumptions are adopted for the surrounding rock prior to establishing the governing equations:

(1) The surrounding rock is homogeneous, continuous, and isotropic;
(2) The moisture content in the surrounding rock exists only in the gaseous and liquid phases, and phase change to ice is not considered;

(3) Water vapor is treated as an ideal gas, obeying the ideal gas law;
(4) Local thermal and moisture equilibrium is assumed at every point within the surrounding rock;
(5) The geometry of the surrounding rock is simplified to a regular form, with one-dimensional heat and moisture transfer along the thickness direction;
(6) The effects of capillary hysteresis during isothermal sorption and desorption are neglected;
(7) The surrounding rock is located within the geothermal zone of constant temperature, and seasonal variations in atmospheric temperature are not considered in the initial temperature distribution.

(1) Governing Equations of Surrounding Rock

(1.1) Moisture transfer

The moisture within the surrounding rock comprises two distinct phases: liquid water and water vapor. Liquid water is transported by capillary action, and its permeation flow obeys Darcy's law [16–19]. Water vapor, on the other hand, is transferred primarily under a partial pressure gradient, and its diffusive transport follows Fick's law [20,21]. Based on the principle of mass conservation, the moisture balance equation for the surrounding rock can be expressed as follows:

$$\frac{\partial w}{\partial \tau} = -\nabla(\vec{J}_l + \vec{J}_v) \tag{1}$$

where w denotes volumetric moisture content of the surrounding rock, kg/m^3; $\vec{J}_l$ is the liquid water transfer, kg/(m^2·s); $\vec{J}_v$ is the water vapor transfer, kg/(m^2·s).

According to Darcy's law, the calculation formula for the flux of liquid water is as follows:

$$\vec{J}_l = K_l \nabla S \tag{2}$$

where K_l denotes conductivity coefficient of liquid water, kg/(m·s·Pa); S is capillary pressure, Pa.

The conductivity coefficient of liquid water, being difficult to determine directly, can be calculated using the following formula:

$$K_l = \frac{\delta_v \varphi P_{sat}}{R_v \cdot (T - 273.15) \cdot \rho_w} \tag{3}$$

where R_v is the gas constant for water vapor, taken as 462 J/(kg·K); T is the thermodynamic temperature, K; ρ_w is the density of liquid water, assumed as 1000 kg/m^3.

The capillary force in Equation (2) can be converted into volumetric moisture content and relative humidity based on the materials' isothermal sorption equilibrium curve, translating capillary pressure gradient into a relative humidity gradient. The formula is as follows:

$$\nabla S = \frac{dS}{dw} \cdot \frac{dw}{d\varphi} \nabla \varphi \tag{4}$$

where φ is relative humidity of the material.

$\xi = \frac{dw}{d\varphi}$ represents the slope of the isothermal moisture absorption equilibrium curve of the material. The final expression of the formula for calculating the amount of liquid water migration is as follows:

$$\vec{J}_l = K_l \frac{dS}{dw} \cdot \frac{dw}{d\varphi} \nabla \varphi = -D_w \xi \nabla \varphi \tag{5}$$

where $D_w = -K_l \frac{dS}{dw}$ is diffusion coefficient of liquid water, m^2/s.

According to Fick's law, the migration amount of water vapor is calculated as:

$$\vec{J}_v = -\delta_v \nabla P_v \tag{6}$$

where δ_v is the water vapor permeability coefficient, kg/(m·s·Pa); $P_v = \varphi P_{sat}$ is the water vapor partial pressure, Pa; P_{sat} is the saturated water vapor pressure.

Since the saturated vapor pressure depends solely on temperature, it can be computed by the following formula:

$$P_{sat} = 610.5 \exp\left(\frac{17.269(T - 273.15)}{T - 35.85}\right) \tag{7}$$

Converting the water vapor pressure gradient into gradients of relative humidity and temperature, the formulas are:

$$\nabla P_v = P_{sat} \nabla \varphi + \varphi \nabla P_{sat} \tag{8}$$

$$\nabla P_{sat} = \frac{dP_{sat}}{dT} \nabla T \tag{9}$$

By substituting Equations (8) and (9) into Equation (6), the expression for the water vapor migration rate can be derived as follows:

$$\vec{J}_v = -\delta_v \left(P_{sat} \nabla \varphi + \varphi \frac{dP_{sat}}{dT} \nabla T\right) \tag{10}$$

Replacing Equations (5) and (10) into (1), the moisture balance equation takes the form:

$$\begin{aligned} \xi \frac{\partial \varphi}{\partial \tau} &= \frac{\partial}{\partial x}\left[D_w \xi \nabla \varphi + \delta_v \left(P_{sat} \nabla \varphi + \varphi \frac{dP_{sat}}{dT} \nabla T\right)\right] \\ &= \frac{\partial}{\partial x}\left[\left(D_w \xi + \delta_v P_{sat}\right) \frac{\partial \varphi}{\partial x} + \delta_v \varphi \frac{dP_{sat}}{dT} \frac{\partial T}{\partial x}\right] \end{aligned} \tag{11}$$

Finally, the moisture balance equation of the surrounding rock can be simplified as follows:

$$\xi \frac{\partial \varphi}{\partial \tau} = \frac{\partial}{dx}\left(D_\varphi \frac{\partial \varphi}{\partial x} + D_T \frac{\partial T}{\partial x}\right) \tag{12}$$

where $D_\varphi = D_w \xi + \delta_v P_{sat}$ is the mass transfer coefficient induced by the gradient of relative humidity, kg/(m·s); $D_T = \delta_v \varphi \frac{dP_{sat}}{dT}$ is the mass transfer coefficient induced by the temperature gradient, $m^2/(s \cdot K)$.

(1.2) Heat transfer

The heat transfer process in surrounding rock, aside from heat transfer during the moisture migration phase, may also include the latent heat released during phase changes in moisture. Therefore, the heat transfer in the surrounding rock primarily comprises three components: heat conduction of the surroundings, energy carried by moisture migration, and latent heat associated with moisture phase changes. Accordingly, the total heat flux can be described by the following equation:

$$q = -\lambda \nabla T + c_v T \vec{J}_v + c_w T \vec{J}_l + L(T) \vec{J}_v \tag{13}$$

where q is the total heat flux, W/m^2; λ is the effective thermal conductivity coefficient of the material, W/(m·K); c_v is the specific heat capacity of water vapor, J/(kg·K); c_w is the specific heat capacity of liquid water, taken as 4200 J/(kg·K); $L(T)$ is the latent heat of vaporization, J/kg.

Since the latent heat of vaporization depends directly on temperature, the relationship can be expressed as follows:

$$L(T) = [2500 - 2.4(T - 273.15)] \times 10^3 \tag{14}$$

Given that the sensible heat component of moisture is significantly smaller than the latent heat component, the heat transfer caused by liquid water and water vapor migration can be neglected in the calculation of heat flux in the surrounding rock. Consequently, the simplified formula becomes as follows:

$$q = -\lambda \nabla T + L(T) \vec{J}_v \tag{15}$$

According to the law of conservation of energy, the thermal equilibrium equation of the surrounding rock is as follows:

$$(c_s \rho_s + c_w w) \frac{\partial T}{\partial \tau} = -\nabla q \tag{16}$$

where ρ_s is the dry density of the surrounding rock, kg/m^3; c_s is the specific heat capacity at constant pressure in a dry state, J/(kg·K).

Substituting Equations (10), (14) and (15) into Equation (16), the formula can be transformed into the following formula:

$$(c_s \rho_s + c_w w) \frac{\partial T}{\partial \tau} = \frac{\partial}{dx} \left[(\lambda + L(T) \delta_v \varphi \frac{dP_{sat}}{dT} \nabla T + L(T) \delta_v P_{sat} \nabla \varphi \right] \tag{17}$$

The ultimate form of the thermal balance equation for the surrounding rock simplifies as follows:

$$(c_s \rho_s + c_w w) \frac{\partial T}{\partial \tau} = \frac{\partial}{dx} \left(\lambda_{eff} \frac{\partial T}{\partial x} + J_\varphi \frac{\partial \varphi}{\partial x} \right) \tag{18}$$

where $\lambda_{eff} = \lambda + L(T) \delta_v \varphi \frac{dP_{sat}}{dT}$ is the effective thermal conductivity coefficients of the surrounding rock, W/(m·K); $J_\varphi = L(T) \delta_v P_{sat}$ is the heat transfer coefficient induced by the gradient of relative humidity.

(2) Governing equations of moisture air

(2.1) Moisture transfer

The axial air moisture transfer in tunnel can be regarded as a one-dimensional unsteady convective moisture transfer problem with internal moisture source. The governing equation is expressed as follows:

$$A \rho_{air} \frac{\partial d_f}{\partial \tau} + A \rho_{air} v \frac{\partial d_f}{\partial x} = h_m U \left(P_w - P_f \right) + M_s + M_{in} \tag{19}$$

where d_f is the specific humidity of the tunnel air, kg/kg; h_m is the convective mass transfer coefficient at the tunnel's surrounding rock surface, s/m; P_w is the vapor partial pressure at the surface of the tunnel rock wall, Pa; P_f is the vapor partial pressure of the tunnel air, Pa; M_s is the internal moisture source within the tunnel, given the relatively small moisture source inside the tunnel, this term can be neglected, thus its value is considered zero in this study, kg/(m·s); M_{in} is the moisture exchange rate between the tunnel and the external atmosphere, kg/(m·s).

The specific air humidity can be represented using the total pressure and water vapor partial pressure as follows:

$$d_f = 0.622\frac{P_f}{B - P_f} \tag{20}$$

Let $b = \frac{\partial d_f}{\partial P_f} = 0.622\frac{B}{(B-P_f)^2}$, then $\frac{\partial d_f}{\partial \tau} = \frac{\partial d_f}{\partial P_f}\cdot\frac{\partial P_f}{\partial \tau} = b\frac{\partial P_f}{\partial \tau}$, $\frac{\partial d_f}{\partial x} = \frac{\partial d_f}{\partial P_f}\cdot\frac{\partial P_f}{\partial x} = b\frac{\partial P_f}{\partial x}$. The final moisture balance equation for moist air becomes as follows:

$$Ab\rho_{air}\frac{\partial P_f}{\partial \tau} + A\rho_{air}vb\frac{\partial P_f}{\partial x} = h_m U\left(P_w - P_f\right) + M_s + M_{in} \tag{21}$$

Since the internal moisture source is relatively small, it is omitted in this formulation. The moisture exchange between the tunnel and the external environment via the shaft is described by the following formula:

$$M_{in} = \pm\frac{A\rho_{air}vd}{L} \tag{22}$$

where d is the specific humidity of the air, for exhaust ventilation, the air temperature inside the tunnel is used, and for intake ventilation, the outside ambient air temperature is used, kg/kg. When the tunnel is in exhaust mode, moisture is expelled outward, and a negative sign is applied, and when in intake mode, fresh outside air introduces moisture into the tunnel, and a positive sign is used.

(2.2) Heat transfer

The axial air heat transfer in the tunnel can be modeled as a one-dimensional unsteady convective heat transfer problem with internal heat source. The governing equation is as follows:

$$A\rho_{air}c_p\frac{\partial T_f}{\partial \tau} + A\rho_{air}c_pv\frac{\partial T_f}{\partial x} = h_m U\left(T_w - T_f\right) + Q_s + Q_{in} \tag{23}$$

where A is the cross-sectional area of the tunnel, m^2; ρ_{air} is the air density, kg/m^3; c_p is the specific heat capacity of air, $J/(kg{\cdot}K)$; T_f is the air temperature in the tunnel, K; v is the velocity of piston wind inside the tunnel, m/s; h is the convective heat transfer coefficient between the tunnel air and the surrounding rock wall, $W/(m^2{\cdot}K)$; U is the perimeter of the tunnel cross-section, m; T_w is the temperature of the surrounding rock wall, K; Q_s is the internal heat source per unit length of the tunnel, W/m; Q_{in} is the heat exchange between the tunnel and the external atmosphere, W/m.

The internal heat sources include train braking heat generation, train starting resistance heat, acceleration heat, movement heat, vehicle resistance heat, heat emission from the train's air conditioning system, air resistance heat, and tunnel equipment heat dissipation. Using the fundamental parameters of a subway system provided in reference [22], the heat sources within the tunnel are calculated, with detailed parameters listed in Table 1. After computation, the average heat generation within the tunnel is determined to be 153.57 W/m per unit time and per unit length of the tunnel.

Table 1. Basic parameter table of the subway.

Parameter	Value	Unit
metro train length	120	m
metro train cross-sectional area	10.6	m^2
metro train cross-sectional perimeter	13.2	m
metro train formation	6 (4M2T)	car
motor car weight	35	t
trailer car weight	31	t
rated passenger capacity	300	p/car
average passenger weight	60	Kg
constant travel speed	80	km/h
maximum acceleration	0.83	m/s^2
maximum deceleration	0.94	m/s^2
peak-hour train service frequency	30	pph
air conditioning cooling capacity	70	KW/car

The heat exchange between the tunnel and the outside environment via the ventilation system is described by the following formula:

$$Q_{in} = \pm \frac{A\rho_{air}c_p vt}{L} \tag{24}$$

where t is the air temperature. For exhaust air, the tunnel air temperature is used, and for incoming air, the outdoor air temperature is used, °C. L is the length of the tunnel affected by the intake or exhaust airflow, m. When the tunnel is in exhaust mode, it dissipates heat outward, and the formula uses a "–", and when in intake mode, fresh external air cools the tunnel, and the formula uses a "+".

(3) Initial and boundary conditions

(3.1) Initial conditions

The underground structure studied in this paper is located in the constant temperature layer, which is generally considered to have a temperature roughly equal to the local annual mean surface temperature, as referenced in the literature [23]. Due to the unique microclimate and the presence of groundwater, the surrounding rock exhibits higher moisture content. Therefore, the initial relative humidity of the surrounding rock is assumed to be 85%.

$$\begin{cases} T(x,\tau)|_{\tau=0} = T_0 \\ \varphi(x,\tau)|_{\tau=0} = \varphi_0 \end{cases} \tag{25}$$

The initial air temperature and humidity are set at 20 °C and 60%, respectively, with the initial moisture content of the air calculated to be 8.73 g/kg.

(3.2) Boundary conditions

The boundary conditions for the mathematical model of the coupled heat and moisture transfer equation in surrounding rock include internal boundary conditions and far-field boundary conditions. The heat and moisture exchange between the inner surface of the surrounding rock and the air within underground structures largely depends on the temperature difference, water vapor pressure difference, and the convective heat and mass

transfer coefficients between them. The internal boundary condition is characterized as a convective boundary, as shown in Equation (26):

$$\begin{cases} \left(-D_\varphi \dfrac{\partial \varphi}{\partial x} - D_T \dfrac{\partial T}{\partial x}\right)_{x=0} = h_m(\varphi_{in} P_{sat,in} - \varphi_{x=0} P_{sat,x=0}) \\ \left(\lambda_{eff} \dfrac{\partial T}{\partial x} + J_\varphi \dfrac{\partial \varphi}{\partial x}\right)_{x=0} = h \cdot (T_{in} - T_{x=0}) \end{cases} \tag{26}$$

The far-field boundary is located at a depth within an effectively semi-infinite object, where the temperature and humidity are virtually unaffected by heat and moisture transfer, remaining at their initial states. Therefore, the far boundary is set as a boundary with fixed temperature and humidity, with its thickness determined according to the formula provided in reference [24].

$$\begin{cases} T_{x\to\infty} = T_0 \\ \varphi_{x\to\infty} = \varphi_0 \end{cases} \tag{27}$$

where h_m is the convective mass transfer coefficient for the surface, s/m; h is the convective heat transfer coefficient for the surface, W/(m^2·K); φ_{in} is the indoor relative humidity; $P_{sat,in}$ is the indoor saturation vapor pressure, Pa; $\varphi_{x=0}$ is the surface relative humidity; $P_{sat,x=0}$ is the surface saturation vapor pressure, Pa; T_{in} is the indoor temperature, K; $T_{x=0}$ is the surface temperature, K; $T_{x\to\infty}$ is the far boundary temperature, K; $\varphi_{x\to\infty}$ is the far boundary relative humidity.

For the convective heat transfer coefficient, the related literature presents various empirical formulas and recommended values. For natural convection, the recommended convective heat transfer coefficients from reference [25] are 3 W/(m^2·K) for walls, 4.3 W/(m^2·K) for ceilings, and 1.5 W/(m^2·K) for the ground. Pedersen [26] provides a calculation formula for convective heat transfer coefficients when wind speeds are below 5 m/s: $h = 5.82 + 3.96v$. EN15026 [27] similarly offers a formula for convective heat transfer coefficients under wind speeds less than 5 m/s: $h = 4 + 4v$. Reference [28] reports an empirical value of 7.7 W/(m^2·K) for the convective heat transfer coefficient.

For the convective heat transfer coefficient at the tunnel surrounding rock wall surface, the airflow within the tunnel can be approximated as fully developed flow in a smooth circular pipe, satisfying the equations governing flow in a forced laminar flow. Due to minor variations in the Prandtl number within the tunnel, and considering the influence of wall roughness, the convective heat transfer coefficient for the tunnel wall is calculated using the following formula [29]:

$$h = 0.045 \frac{\lambda}{d^{0.2}} \cdot \left(\frac{v \rho_a}{\mu}\right)^{0.8} \tag{28}$$

where λ is the thermal conductivity of air, W/(m·K); d is the hydraulic diameter of the tunnel cross-section, m; v is the airflow velocity in the tunnel, m/s; ρ_a is the density of air, kg/m^3; u is the dynamic viscosity of air, N·s/m^2. This formula applies under conditions where the airflow speed exceeds 1 m/s, and for velocities below 1 m/s, the convective heat transfer coefficient of natural ventilation walls is taken as 3 W/(m^2·K).

Currently, both domestically and internationally, the comparable criterion method is primarily employed to calculate the convective mass transfer coefficient. When heat and mass exchange occur simultaneously between the fluid and the wall surface, the relation between the surface convective mass transfer coefficient and the convective heat transfer coefficient must satisfy the following formula:

$$h_m = \frac{h}{\rho_a c_p} Le^{-\frac{2}{3}} \tag{29}$$

where c_p is the specific heat capacity of air at constant pressure, J/(kg·K); *Le* is the Lewis number, which can be approximated as 1.

Consequently, the wall convective heat transfer coefficient can be calculated using the following equation:

$$h_m = 7.7 \times 10^{-9} \times h \tag{30}$$

The variations in temperature and humidity of the air entering through the ventilation shaft are neglected, and the inlet air parameters are assumed to be equal to the outdoor air parameters.

$$\begin{cases} T_f(0,\tau) = T_{out}^{\tau} \\ \varphi_f(0,\tau) = \varphi_{out}^{\tau} \end{cases} \tag{31}$$

2.3. Material Properties

By consulting relevant literature [30], the thermal and hygric physical parameters of concrete and rock–soil materials are obtained, as detailed in Table 2. According to the formulas for material physical properties, it is evident that the thermal conductivity of rock and soil as well as concrete is related to their moisture content. Additionally, their vapor permeability and liquid water conductivity coefficients are influenced by temperature and moisture content. From the perspective of material physical properties, this also indicates that the thermal and hygric transfer processes in surrounding rock are interconnected and mutually influential.

Table 2. Material thermal and moisture physical parameters table.

Material	Volumetric Moisture Content (kg/m^3)	Thermal Conductivity (W/(m · K))	Water Vapor Permeability Coefficient (kg/(m · s · Pa))	Liquid Water Conductivity Coefficient (kg/(m · s · Pa))
soil	$38.4\phi^{15.2} + 60\phi^{0.45}$	$0.79 + \frac{1.98}{1000}w$	$\frac{2.13 \times 10^{-6}}{R_v T}$	$\frac{\delta_v \varphi P_{\text{sat}}}{R_{\text{v}} \cdot (T - 273.15) \cdot \rho_{\text{w}}}$
concrete	$\frac{146}{\left(1+\left(-8\times10^{-8}\cdot\frac{RT\rho_w}{M_w}\ln(\varphi)\right)^{1.6}\right)^{0.375}}$	$1.5 + \frac{15.8}{1000}w$	$\frac{M_w}{RT}\frac{26.1 \times 10^{-6}}{200}\frac{1-\frac{w}{146}}{0.5(1-\frac{w}{146})^2+0.5}$	$\exp[-39.26 + 0.07(w-73) -1.74\times10^{-4}(w-73)^2 -2.8\times10^{-6}(w-73)^3 -1.16\times10^{-7}(w-73)^4 +2.6\times10^{-9}(w-73)^5]$

3. Model Implementation and Validation

3.1. The Implementation of the Numerical Model

The mathematical model governing the coupled heat and moisture transfer in surrounding rock consists of partial differential equations with variable coefficients. Their strong nonlinearity and tight coupling make it difficult to derive an analytical solution directly. Therefore, a numerical approach is adopted. The finite volume method (FVM) is employed in this work due to its physically meaningful discretization—each control volume is associated with a nodal point, ensuring flux conservation across the domain. Moreover, the method facilitates a relatively straightforward treatment of boundary conditions [31]. In this paper, the FVM is applied to discretize the coupled heat and moisture transfer model. The region is discretized using an exterior-node layout. Under non-uniform grid conditions, this approach achieves higher accuracy than interior-node methods. Nodes are also specified at material interfaces to address parameter discontinuities and enhance numerical precision. For the transient solution, a fully implicit scheme is adopted, which offers unconditional stability and improved convergence.

In this study, the mathematical model is solved numerically using MATLAB R2021a programming. The computational procedure begins with the definition of known param-

eters, followed by the specification of spatial and temporal discretization steps and the generation of the computational grid. A time-stepping scheme is employed to advance the solution, in which the temperature, relative humidity, and moisture content at all nodal points are computed layer by layer at each time step. Due to the nonlinear nature of the governing equations, the coefficient matrix depends on the unknown temperature and relative humidity fields. To address this, an iterative solution strategy is adopted: at each time step, the coefficient matrix is updated using the temperature and humidity values from the previous iteration as provisional estimates, thereby linearizing the system of equations. This linearized system is then solved iteratively until the differences in temperature and relative humidity between successive iterations fall below a prescribed convergence tolerance. The resulting values are taken as the solution for the current time step. This process is repeated sequentially, enabling the full numerical simulation of the coupled heat and moisture transfer in the surrounding rock.

The above solution process obtained the key boundary parameters such as the heat and moisture exchange flux on the inner wall of the tunnel, which laid the foundation for the solution of the air heat and moisture state in the tunnel. In this paper, the finite volume method is used to discretize the air heat and moisture balance equation. As shown in Figure 3, the internal nodes are used to divide the solution area. The unsteady term is calculated by the fully implicit scheme, and the convective term is calculated by the upwind difference scheme. Through the discretization of the air heat and moisture balance equation, it can be expressed as follows:

$$A_{fP}T_{fP} = A_{fW}T_{fW} + A^0_{fP}T^0_{fP} + S_{f1} \tag{32}$$

$$B_{fP}P_{fP} = B_{fW}P_{fW} + B^0_{fP}P^0_{fP} + S_{f2} \tag{33}$$

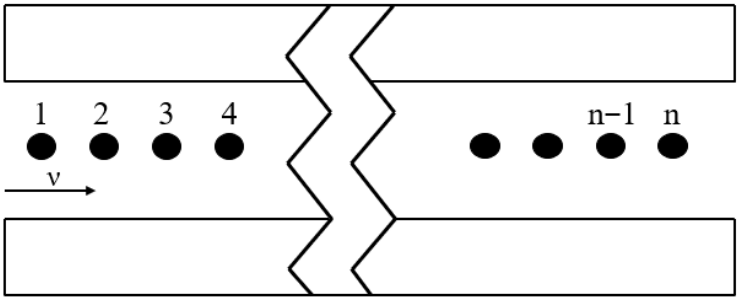


Figure 3. The node division diagram of tunnel air.

3.2. The Validation of the Numerical Model

To validate the reliability of the proposed model, this study selects benchmark cases involving both single-layer and multi-layer materials, comparing the numerical results with analytical solutions available in the literature.

For the single-layer material validation, two established benchmark cases—EN-15026 and HAMSTAD2—were employed. The EN-15026 case considers a semi-infinite porous material heated and humidified on the left side. The initial temperature and relative humidity of the material are set to 20 °C and 50%, respectively. The left boundary is maintained at a constant temperature of 30 °C and 95% relative humidity, while the right boundary is treated as extending to infinity, preserving the initial conditions. The model simulates the temperature and humidity variations over one year, and the internal temperature and volumetric moisture content distributions at 7, 30, and 365 days are extracted for comparison with reference data [27]. As illustrated in Figure 4, the numerical

results show excellent agreement with those reported in the literature, with a maximum deviation of only 2%.

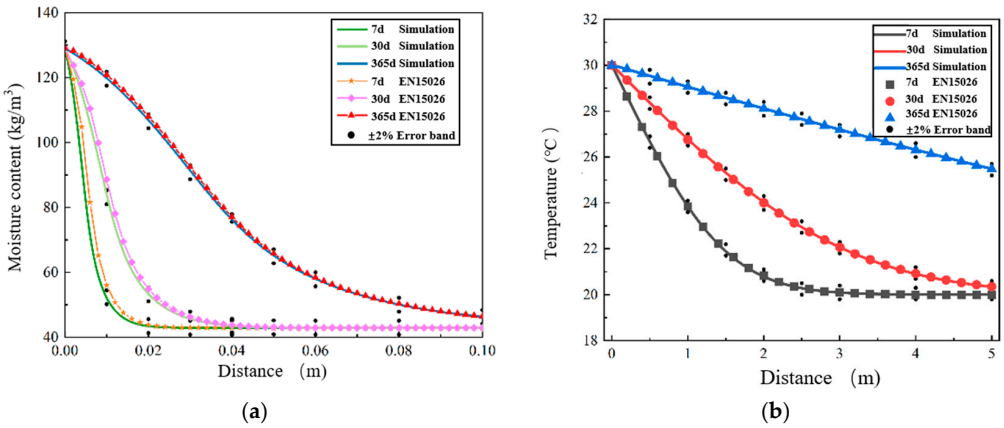


Figure 4. EN-15026 case verification: (**a**) Volumetric moisture content; (**b**) Temperature.

The HAMSTAD2 benchmark case examines the evolution of moisture content during the isothermal drying of a single-layer wall with a thickness of 0.2 m. The initial temperature is set to 20 °C, and the initial moisture content is 84.77 kg/m^3, which corresponds to a relative humidity of approximately 95% according to the material's sorption isotherm. Indoor and outdoor relative humidity values are maintained at 45% and 60%, respectively, with convective heat transfer coefficients of 25 W/(m^2·K) applied on both surfaces. The simulated distributions of volumetric moisture content at 100, 300, and 1000 h are presented in Figure 5 [32], demonstrating close agreement with reference data from the literature and thereby validating the accuracy of the numerical model.

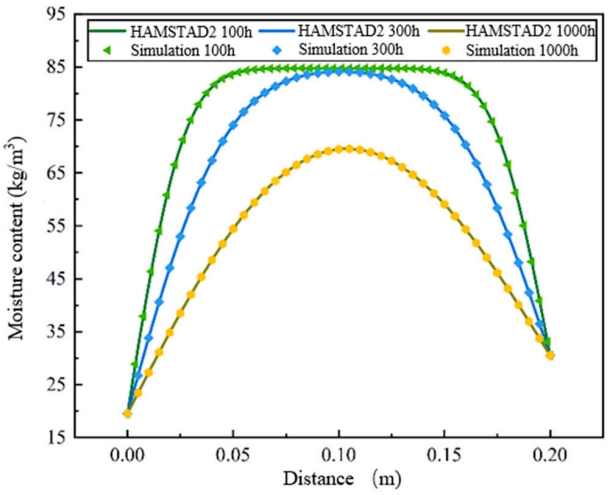


Figure 5. HAMSTAD2 case verification: volume moisture content.

For multilayer materials, the HAMSTAD5 case was selected, examining a wall composed of 365 mm brick, 15 mm mortar layer, and 40 mm insulation layer. The initial temperature and humidity are 25 °C and 60%. Indoor and outdoor air temperatures are 20 °C and 0 °C, with relative humidities of 60% and 80%, respectively. The indoor convective heat transfer coefficient is 8 W/(m^2·K), and the convective mass transfer coefficient is 5.9×10^{-8} s/m. The thermal and moisture physical parameters of each layer of material can be found in the literature [32]. The outdoor convective heat and mass transfer coefficients are 25 W/(m^2·K) and 1.84×10^{-7} s/m, respectively. The comparison between the relative

humidity and moisture content distributions obtained from the HAMSTAD5 case and the current simulation, as illustrated in Figure 6, shows strong congruence.

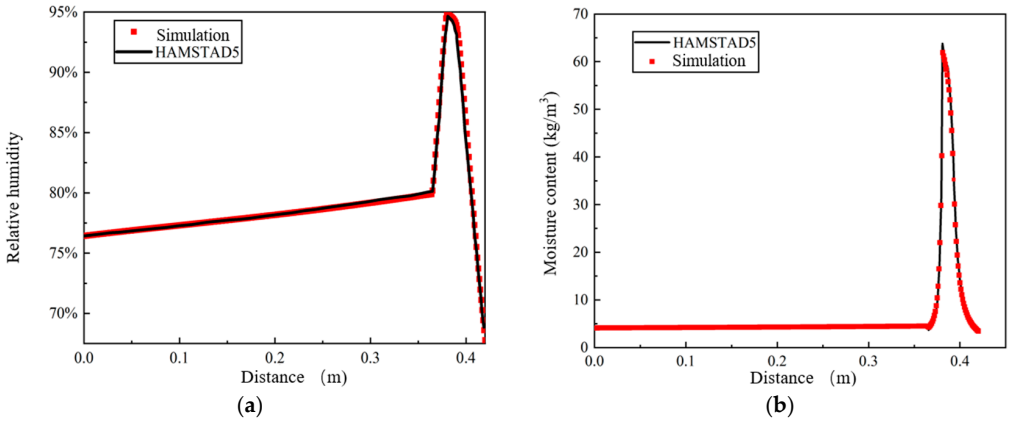


Figure 6. HAMSTAD5 case verification: (**a**) Relative humidity; (**b**) Volumetric moisture content.

Through the validation of these three cases, it is demonstrated that the numerical simulation results of this study are credible and suitable for subsequent research endeavors.

4. Results and Discussion

4.1. Climatic Characteristics of Typical Cities in Different Climatic Regions

Given that the freezing process in surrounding rock is not considered in the established coupled heat and moisture transfer model, this study does not address the thermal-moisture environment of metro tunnels in severely cold regions. Instead, Beijing, Shanghai, Guangzhou, and Kunming are selected as representative cities from the cold, hot summer/cold winter, hot summer/warm winter, and temperate climate zones, respectively. Figure 7 illustrates the variation in daily mean air temperature over time for these cities. The results indicate that the maximum daily mean temperatures descend in the order of Shanghai, Guangzhou, Beijing, and Kunming, while the minimum values follow the sequence of Guangzhou, Kunming, Shanghai, and Beijing. Notably, Beijing's minimum daily mean temperature drops below 0 °C, and the city experiences the largest annual temperature amplitude of 33.54 °C, in contrast to Kunming, which shows the smallest fluctuation of 14.08 °C. Figure 8 presents the hourly moisture content data for the four cities. Based on the recorded air temperature and moisture content, the relative humidity for each city is derived using psychrometric chart analysis.

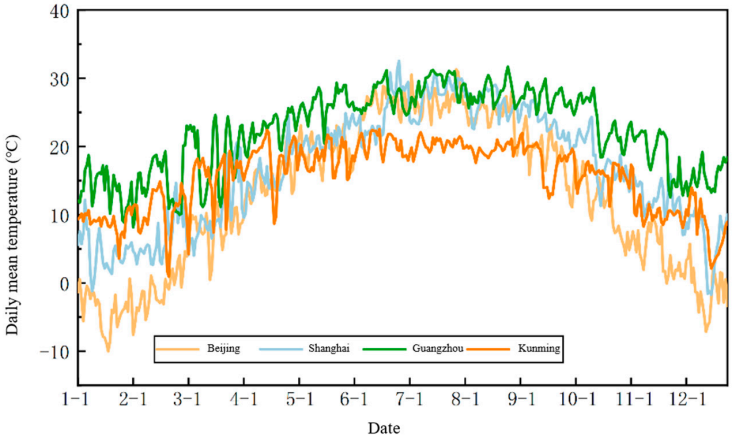


Figure 7. The annual average daily temperature of the four cities.

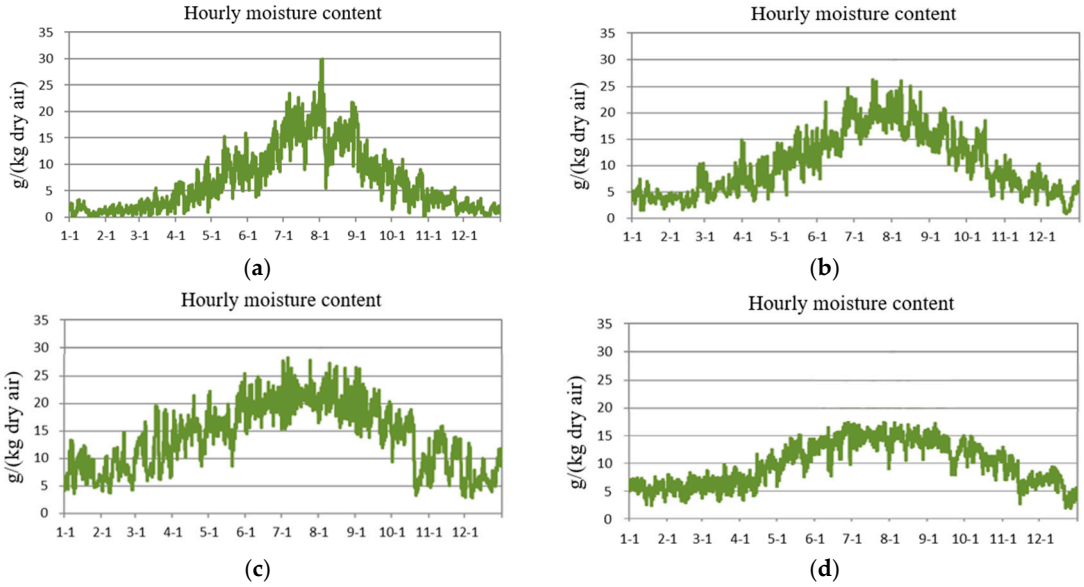


Figure 8. Hourly moisture content throughout the year of the four cities: (**a**) Beijing; (**b**) Shanghai; (**c**) Guangzhou; (**d**) Kunming.

4.2. Interannual Variation in Thermal and Humid Environment of Metro Tunnels in Beijing

Taking the Beijing metro tunnel as a case study, Figure 9 illustrates the longitudinal variation in air temperature and relative humidity inside the tunnel over a 20-year period. As the distance from the entrance increases, the influence of external climate conditions weakens progressively, leading to a gradual attenuation in the annual fluctuation amplitudes of both air temperature and relative humidity along the tunnel length.

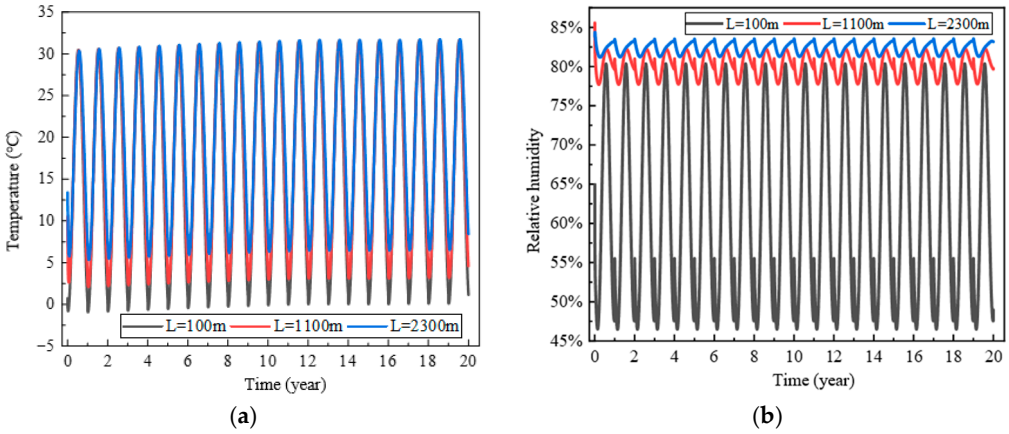


Figure 9. The changes in temperature and humidity of tunnels over 20 years in Beijing: (**a**) Temperature; (**b**) Relative humidity.

As shown in Figure 9a, the minimum air temperature near the tunnel entrance falls below 0 °C. With the accumulation of internal heat sources along the tunnel, the air temperature rises gradually with increasing depth. Temporally, the tunnel air temperature exhibits a year-by-year increasing trend, with the rate of temperature rise slowing over time, while the magnitude of increase becomes more pronounced with greater distance from the entrance. This behavior is attributed to the progressive heat accumulation within the surrounding rock, which reduces its cooling capacity annually. After the operation of the metro tunnels, the continuous heat dissipation from trains and equipment occurs through convective and conductive heat transfer to the surrounding rock. The surrounding rock can only dissipate heat to the tunnel air and the deep natural geothermal gradient, with a

heat transfer rate far lower than the heat input rate, resulting in excess heat being stored as sensible heat. Over time, the temperature difference between the surrounding rock and tunnel air diminishes, weakening the driving force for heat transfer, which ultimately leads to a gradual decline in the rock's cooling capacity.

From Figure 9b, it can be observed that spatially, the relative humidity of the tunnel air increases along the longitudinal direction due to continuous moisture release from the surrounding rock. Temporally, although the humidity source in the tunnel is assumed to follow an approximately periodic inter-annual pattern without long-term trend, a time-lag effect is evident in the occurrence of the annual peak relative humidity values. This is because, on one hand, with the annual rise in surrounding rock temperature, it takes longer for seasonal fluctuations in external air temperature to influence the tunnel air temperature. Since relative humidity is inversely related to temperature, the occurrence of temperature extremes is progressively delayed each year, directly causing the timing of relative humidity maxima to be postponed as well. On the other hand, the cumulative moisture within the surrounding rock over the years slows down the rate of water exchange between the rock and the air. Only when the temperature fluctuations of the surrounding rock reach greater magnitudes does significant moisture release or storage occur, further delaying the timing of the maximum moisture content. Only when the temperature fluctuations of the surrounding rock reach greater magnitudes does significant moisture release or storage occur, further delaying the timing of the maximum atmospheric moisture in the tunnel air.

Figure 10a illustrates the spatial distribution of air temperature and relative humidity along the tunnel length on a typical day in Year 20. A temperature differential of 0.47 °C and a relative humidity difference of 2.2% are observed between the positions at L = 100 m and L = 2300 m (L = 100 m refers to the place within the tunnel that is 100 m away from the tunnel exit). This relatively small temperature gradient along the tunnel is attributed to the cooling effect exerted by the surrounding rock, which partially offsets the heat accumulation along the longitudinal direction. Figure 10b shows the interannual variation in the peak air temperature inside the tunnel, which exhibits a gradually increasing trend over the 20-year period. The rate of temperature rise decreases year by year, resulting in a total increase of 1.5 °C over two decades, with an average annual increment of 0.075 °C.

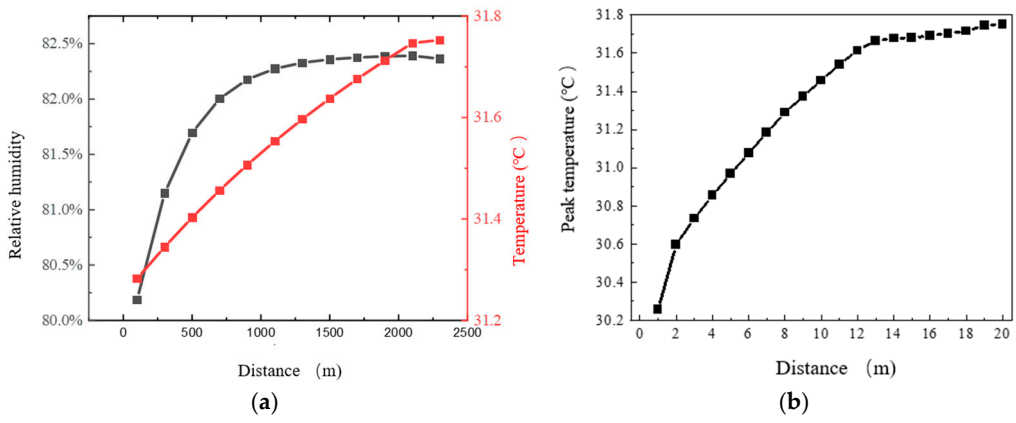


Figure 10. The air temperature and humidity distribution and peak temperature in Beijing: (**a**) Air temperature and humidity distribution; (**b**) Annual peak air temperature.

Figures 11 and 12 present the interannual variations in temperature and relative humidity of the surrounding rock at distances of 100 m and 2300 m along the tunnel. As shown in Figure 11, spatially, the relative humidity of the rock within 0.1 m of the wall surface is strongly influenced by the cyclic variations in tunnel air temperature and humidity, exhibiting significant fluctuation amplitudes that attenuate with increasing depth.

Moisture transport displays a noticeable delay effect, resulting in higher relative humidity at locations farther from the wall surface. Concurrently, due to the longitudinal increase in air relative humidity along the tunnel, the relative humidity of the surrounding rock also exhibits a corresponding rising trend in the downstream direction. Temporally, the relative humidity of the surrounding rock at various depths decreases annually, with the rate of decline gradually slowing over time. After approximately 12 years, the relative humidity near the wall stabilizes dynamically, indicating that the surrounding rock predominantly releases moisture into the airflow.

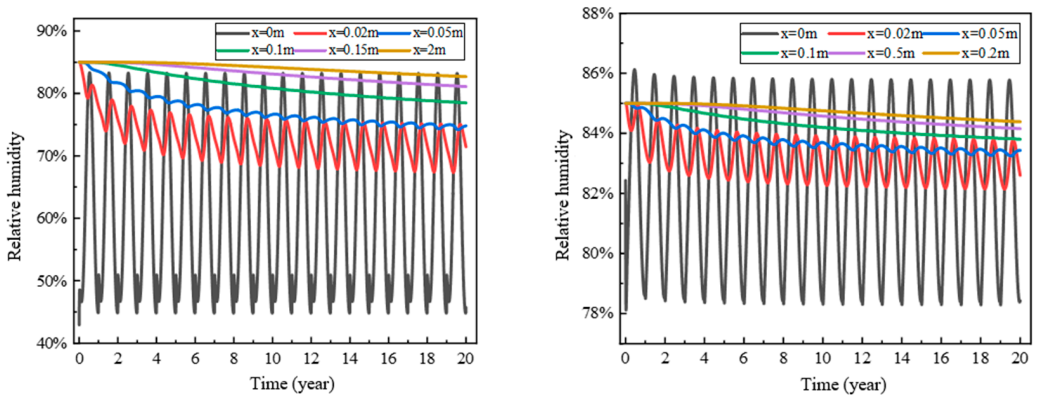


Figure 11. The variation in relative humidity in the surrounding rock over time in Beijing: (**a**) L = 100 m; (**b**) L = 2300 m.

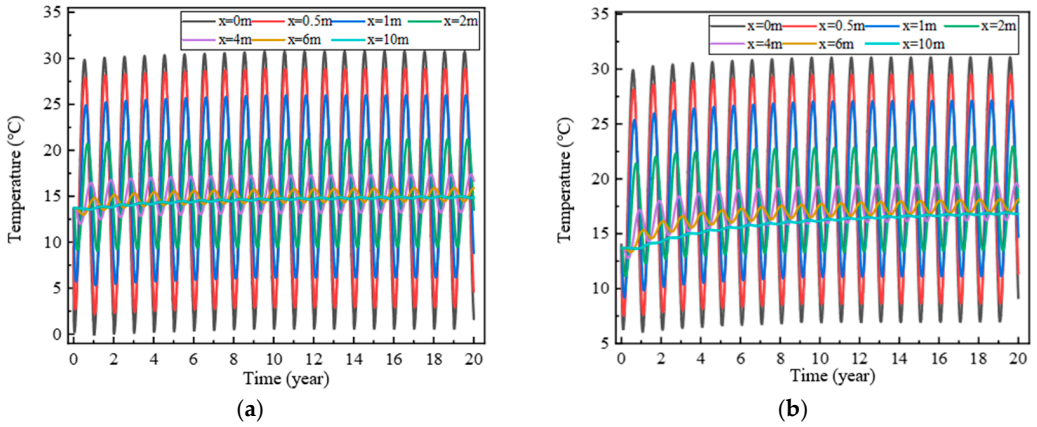


Figure 12. Temperature variations in the surrounding rock in Beijing over time: (**a**) L = 100 m; (**b**) L = 2300 m.

As illustrated in Figure 12, the temperature of the surrounding rock responds seasonally to variations in tunnel air temperature and humidity. Higher heat transfer coefficients at the wall surface lead to faster temperature responses, while locations farther inward exhibit reduced amplitude and a delayed variation pattern. Over time, the temperature of the surrounding rock along the tunnel exhibits a gradually increasing fluctuation trend, indicating that the rock mass primarily acts as a heat sink. The rate of temperature rise slows over time, approaching a state of dynamic equilibrium after about 12 years. In addition, the progressive increase in tunnel air temperature and ongoing heat accumulation contribute to an overall rise in rock temperature and an elevated annual temperature increase rate along the tunnel length.

Over the 20-year operational period, Figures 13 and 14 illustrate the interannual variation in the year-end distributions of relative humidity and temperature in the surrounding

rock at longitudinal positions L = 100 m and L = 2300 m along the tunnel. As shown in Figure 13, the relative humidity distribution within the surrounding rock exhibits limited interannual variation. At the 100 m location, relative humidity decreases progressively from the tunnel wall surface up to a depth of 1.26 m, while beyond 3.4 m, the relative humidity shows a gradual increasing trend over the years. A similar pattern is observed at 2300 m, where relative humidity declines from the wall surface to a depth of 1.62 m, and begins to increase from 4.16 m inward. Figure 14 presents the temperature distributions, revealing the presence of annual temperature peaks within the rock mass. The overall temperature profile initially increases in a near-parabolic manner with depth before stabilizing. The peak temperature values rise year by year, with the peak locations gradually shifting deeper into the rock, reflecting a general warming trend with a progressively declining rate of increase over time.

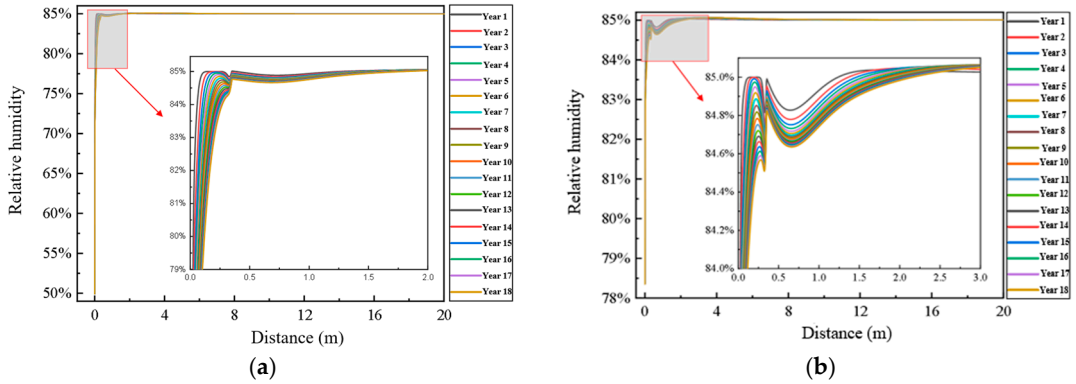


Figure 13. The relative humidity distribution of surrounding rock in Beijing: (**a**) L = 100 m; (**b**) L = 2300 m.

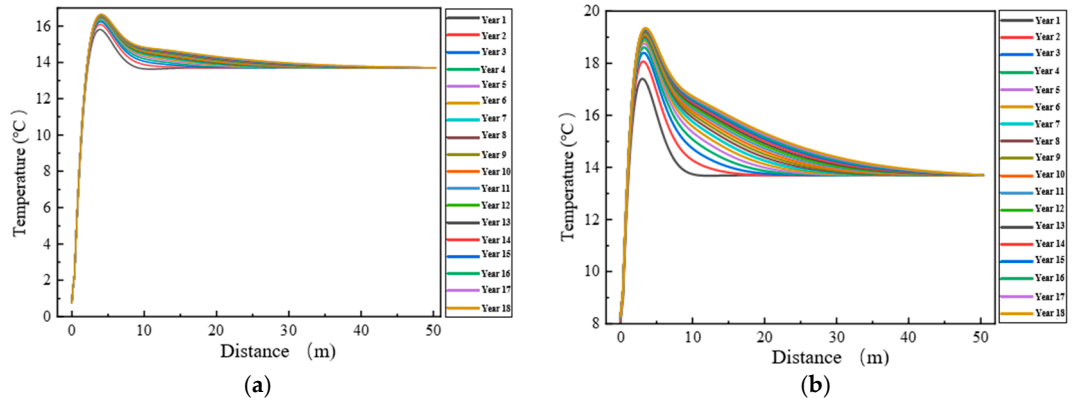
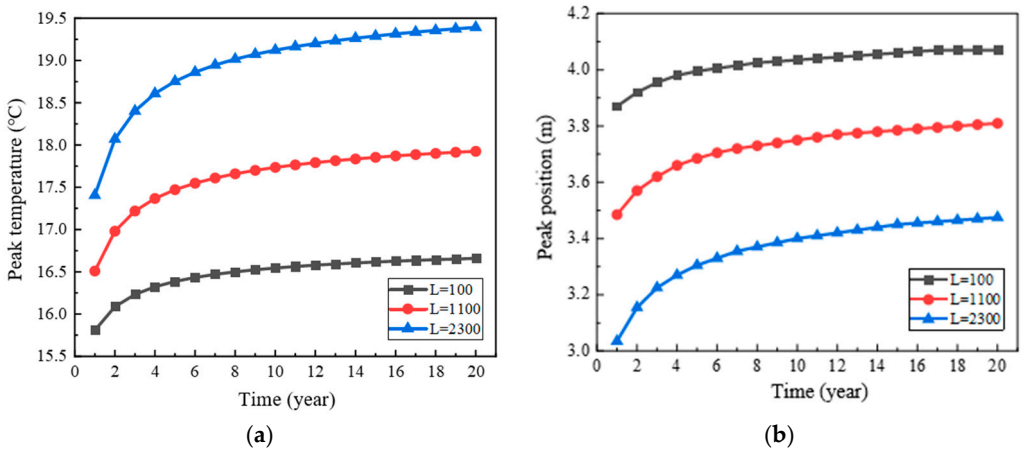


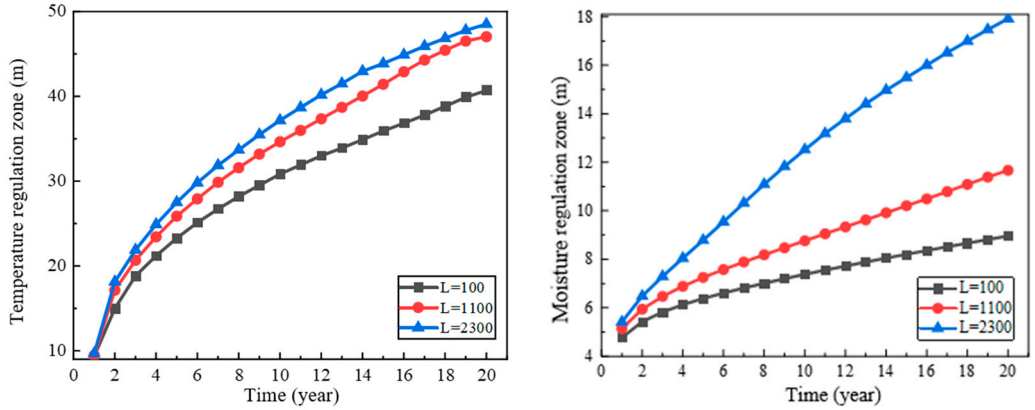
Figure 14. The temperature distribution of surrounding rock in Beijing: (**a**) L = 100 m; (**b**) L = 2300 m.

Under the influence of the tunnel's internal airflow temperature and humidity, distinct variable zones emerge within the surrounding rock, exhibiting significant deviations from the initial thermal and moisture states and following specific variation patterns. These are defined as the "temperature regulation zone" and the "moisture regulation zone." Figures 15 and 16 quantitatively present the interannual variations in the peak temperature of the surrounding rock, the corresponding peak positions, and the annual changes in the thicknesses of the temperature and moisture regulation zones at different locations along the tunnel.



(**a**) (**b**)

Figure 15. Annual variations in peak temperature and position of surrounding rock in Beijing: (**a**) peak temperature; (**b**) peak position.



(**a**) (**b**)

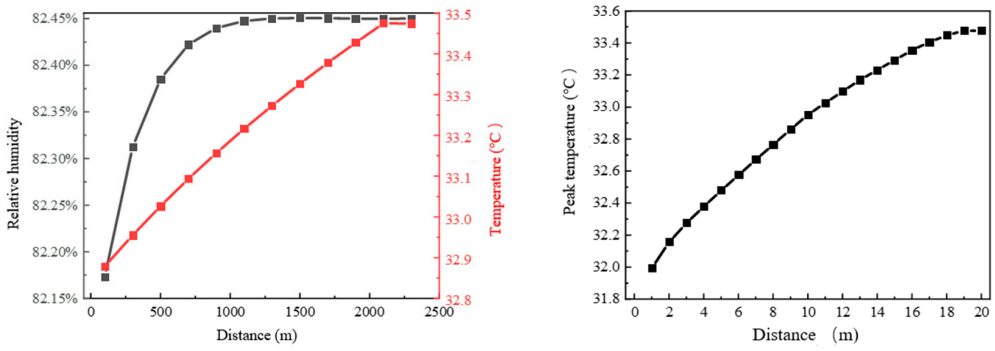
Figure 16. Annual variations in the temperature regulation zone and moisture regulation zone of surrounding rock in Beijing: (**a**) temperature regulation zone; (**b**) moisture regulation zone.

Figure 15 indicates a consistent upward trend in the peak temperature within the surrounding rock over the 20-year period, with a gradually decelerating rate of increase. The peak position also shifts progressively away from the tunnel wall. Specifically, at 100 m, 1100 m, and 2300 m, the peak temperatures increased by 0.9 °C, 1.4 °C, and 2 °C, respectively, corresponding to average annual rises of 0.045 °C, 0.07 °C, and 0.1 °C. The maximum temperature increases relative to the initial conditions reached 3 °C, 4.2 °C, and 5.7 °C. The initial peak locations along the tunnel shifted from 3.87 m to 3.03 m, and by the 20th year, from 4.07 m to 3.48 m. These results collectively demonstrate not only rising peak temperatures and incremental annual growth along the tunnel length but also a decreasing trend in peak location depth in the longitudinal direction.

Figure 16 shows that the thicknesses of both the temperature and moisture regulation zones expand year by year, with the moisture regulation zones consistently thinner than the temperature regulation zones. Over two decades, the temperature regulation zone thicknesses at 100 m, 1100 m, and 2300 m increased from 9.67 m to 40.7 m, 47.04 m, and 48.52 m, respectively, while the moisture regulation zones grew from initial values of 4.77 m, 5.42 m, and 5.42 m to 8.96 m, 11.67 m, and 17.92 m. These patterns suggest that the rising air temperature and humidity along the tunnel drive the progressive thickening of both regulation zones.

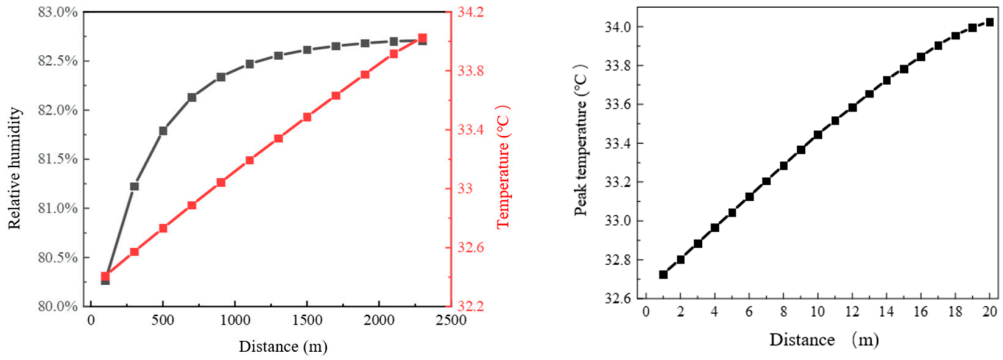
4.3. Interannual Variation in Thermal and Humid Environment of Metro Tunnels in Other Typical Cities

Further analyses were conducted for three additional climatic regions—Shanghai, Guangzhou, and Kunming—to examine spatiotemporal trends in temperature and humidity on typical summer days, interannual variations in tunnel air temperature, and the evolution of regulation zone thickness. Figures 17–19 present the temperature and humidity distributions and peak temperature variations for Shanghai, Guangzhou, and Kunming, respectively.



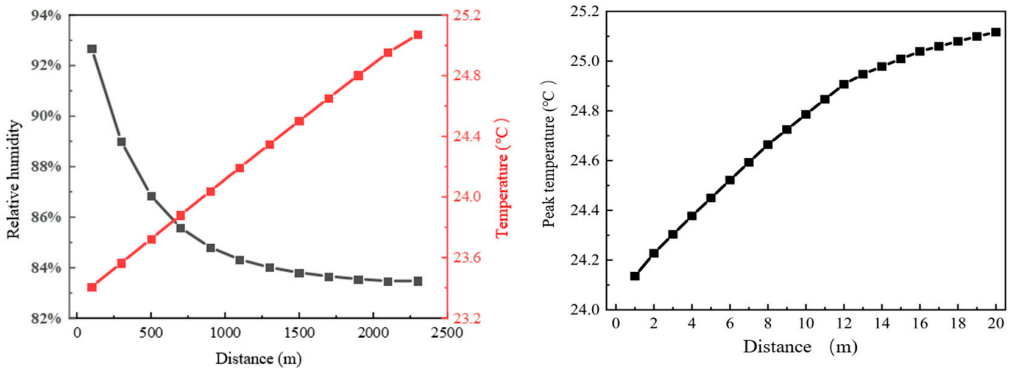
(**a**) (**b**)

Figure 17. The air temperature and humidity distribution and the peak temperature in Shanghai: (**a**) Air temperature and humidity distribution; (**b**) Annual peak air temperature.



(**a**) (**b**)

Figure 18. The air temperature and humidity distribution and the peak temperature in Guangzhou: (**a**) Air temperature and humidity distribution; (**b**) Annual peak air temperature.



(**a**) (**b**)

Figure 19. The air temperature and humidity distribution and the peak temperature in Kunming: (**a**) Air temperature and humidity distribution; (**b**) Annual peak air temperature.

In Shanghai, over the 20-year period, both temperature and relative humidity along the tunnel gradually increased at a decelerating rate. The temperature difference between 100 m and 2300 m was 0.59 °C, with a relative humidity difference of 0.3%. Compared with Beijing, Shanghai exhibits a larger longitudinal temperature gradient but a smaller variation in relative humidity. This is attributed to the initially greater temperature difference between the surrounding rock and the outdoor environment in Beijing, which leads to more pronounced heat absorption and a weaker temperature rise along the airflow path. Additionally, Shanghai experiences relatively minor annual fluctuations in relative humidity. Over the two decades, the average annual increase in air temperature inside the Shanghai tunnel was 0.073 °C. Owing to Shanghai's smaller annual variations in air temperature and humidity compared to Beijing, the resulting environmental changes inside the tunnel are also less marked. In Guangzhou, the tunnel air temperature and relative humidity both increased gradually along the longitudinal direction. The rate of humidity rise diminished progressively along the tunnel, while temperature exhibited an approximately linear relationship with axial distance. Between 100 m and 2300 m, the temperature difference measured 0.61 °C, accompanied by a relative humidity difference of 2.4%. The maximum air temperature inside the tunnel rose annually, showing a near-linear increase over time, with an average annual rise of 0.065 °C. By the 20th year, the peak tunnel air temperature had increased by approximately 1.3 °C. In Kunming, the air temperature along the tunnel increased in an approximately linear manner over time, while relative humidity decreased longitudinally at a diminishing rate. The temperature difference between 100 m and 2300 m reached 1.66 °C, with a relative humidity difference of 9.2%. The maximum air temperature in the Kunming tunnel increased by about 0.98 °C over 20 years, corresponding to an average annual increase of 0.049 °C.

Figures 20–22 present the annual evolution of the temperature and moisture regulation zones within the surrounding rock for Shanghai, Guangzhou, and Kunming. It can be observed that the thicknesses of both the temperature and moisture regulation zones in all three regions exhibit a consistent increasing trend over time, with a progressive thickening along the tunnel length.

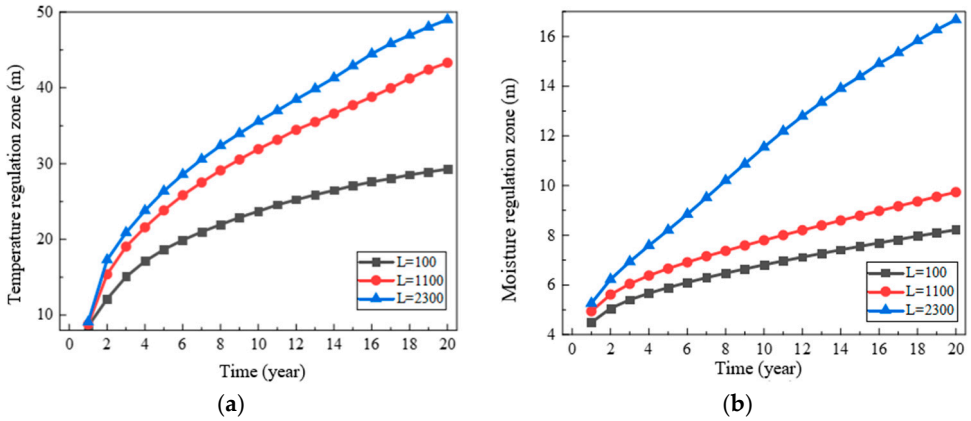


Figure 20. Annual variations in the temperature regulation zone and moisture regulation zone of surrounding rock in Shanghai: (**a**) temperature regulation zone; (**b**) moisture regulation zone.

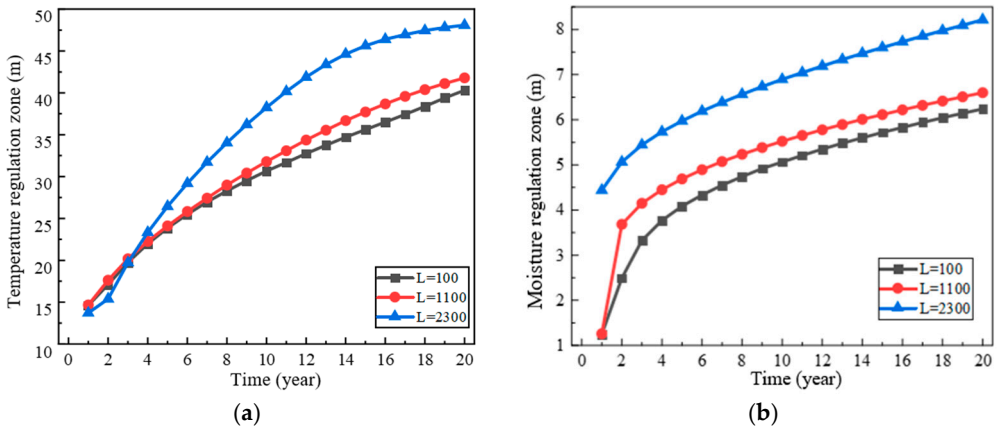


Figure 21. Annual variations in the temperature regulation zone and moisture regulation zone of surrounding rock in Guangzhou: (**a**) temperature regulation zone; (**b**) moisture regulation zone.

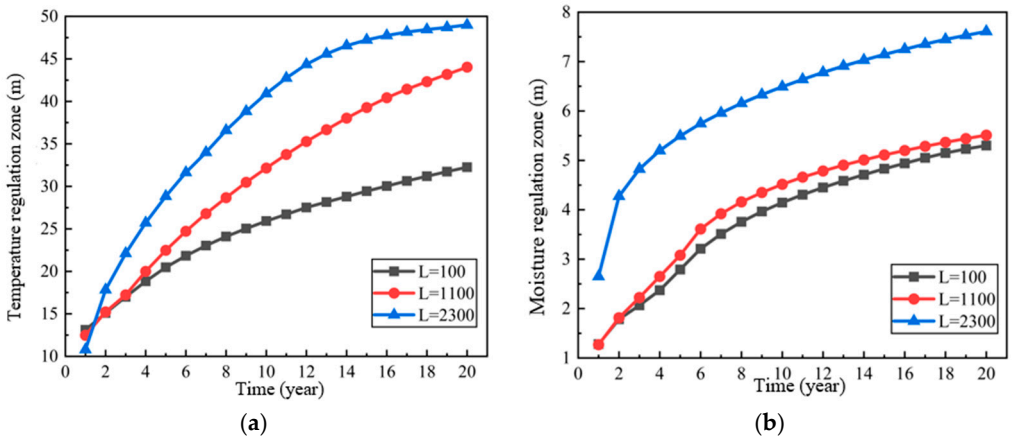


Figure 22. Annual variations in the temperature regulation zone and moisture regulation zone of surrounding rock in Kunming: (**a**) temperature regulation zone; (**b**) moisture regulation zone.

In Shanghai, at longitudinal positions of 100 m, 1100 m, and 2300 m, the thicknesses of the temperature regulation zones expand from initial values of 8.825 m, 9.11 m, and 9.11 m to 29.27 m, 43.31 m, and 48.09 m, respectively. Correspondingly, the moisture regulation zones increase in thickness from 4.49 m, 4.94 m, and 5.26 m to 8.22 m, 9.734 m, and 17.67 m. In Guangzhou, at the same locations, the temperature regulation zones extend from initial values of 14.67 m, 14.67 m, and 13.71 m to 40.31 m, 41.79 m, and 48.09 m. The moisture regulation zones grow from 1.26 m, 1.26 m, and 4.44 m to 6.24 m, 6.6 m, and 8.215 m. In Kunming, the temperature regulation zones at these depths expand from 13.11 m, 12.47 m, and 10.76 m to 32.25 m, 44.02 m, and 48.99 m, while the moisture regulation zones enlarge from 1.28 m, 1.28 m, and 2.65 m to 5.3 m, 5.51 m, and 7.61 m.

4.4. Comparative Analysis of Thermal and Humid Environment of Typical Urban Metro Tunnels in Climatic Regions

This study systematically investigates the interannual evolution of the thermal and humid environments in tunnel sections across four distinct climatic regions. By comparing the annual peak air temperatures inside the tunnels and the corresponding thicknesses of the temperature and moisture regulation zones in the surrounding rock, the influence of regional atmospheric conditions on the tunnel microclimate is elucidated.

As shown in Figure 23, the maximum tunnel air temperatures were highest in Guangzhou, followed by Shanghai, Beijing, and Kunming. Given the strong influence of external climate on the tunnel environment, the magnitude of the air temperature in-

crease over the 20-year period was found to be proportional to the annual amplitude of atmospheric temperature variation, which was most pronounced in Beijing, followed by Shanghai, Guangzhou, and Kunming. These results indicate that higher outdoor peak temperatures lead to elevated tunnel air temperatures, while regions with greater annual temperature fluctuations experience more significant long-term warming within the tunnel.

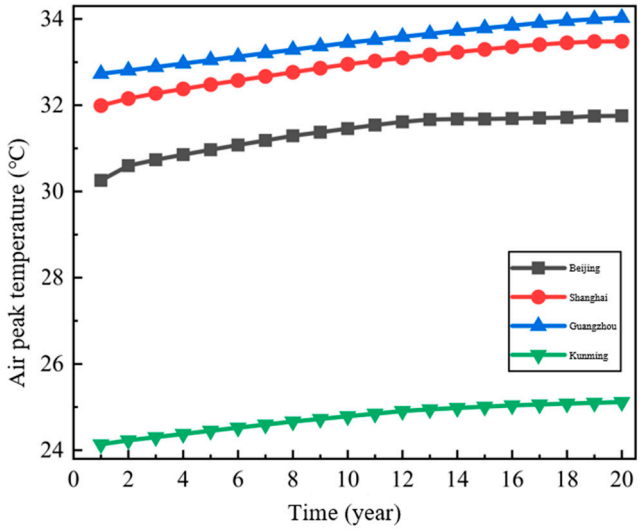


Figure 23. Comparison of the annual peak temperature in four cities.

Figure 24 presents a comparative analysis of the interannual variations in the thicknesses of the temperature and moisture regulation zones within the surrounding rock of the tunnels across the four cities. As shown in Figure 24a, during the initial six-year period, the differences in temperature regulation zone thickness among the cities remain relatively small. Beyond this phase, Kunming consistently develops the most substantial zone thickness. This pattern can be attributed to the larger initial temperature differential between the atmosphere and the surrounding rock in Kunming, which enhances heat exchange and consequently leads to greater development of the regulation zone under comparable conditions. Figure 24b illustrates that the moisture regulation zone thickness decreases in the sequence of Beijing, Shanghai, Guangzhou, and Kunming each year. Furthermore, the temporal growth of moisture regulation zone thickness in Beijing and Shanghai exhibits a near-linear relationship, whereas the progression in Guangzhou and Kunming more closely follows a logarithmic pattern.

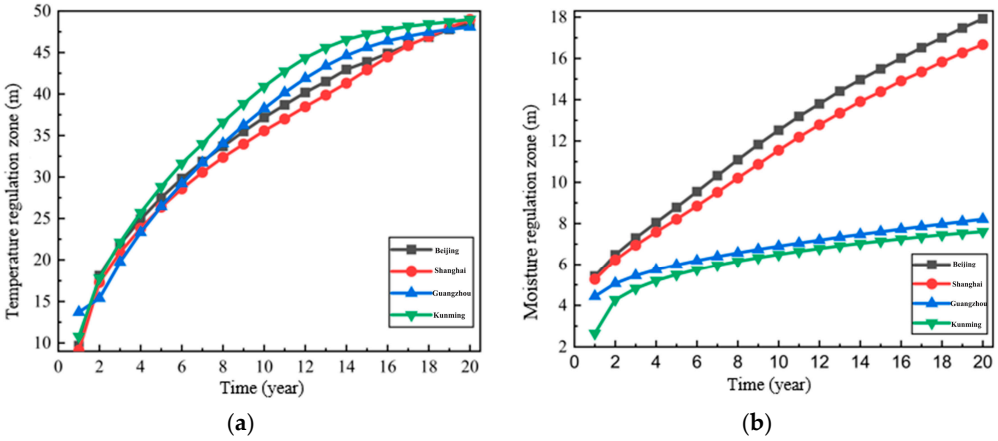


Figure 24. Comparison of the annual temperature and moisture regulation in four cities: (**a**) temperature regulation zone; (**b**) moisture regulation zone.

Figure 25 illustrates the annual rate of change in the thickness of the temperature regulation zone and the moisture regulation zone across four cities. Overall, the data indicate a declining trend in the annual variation rates of both zone thicknesses in all four urban areas.

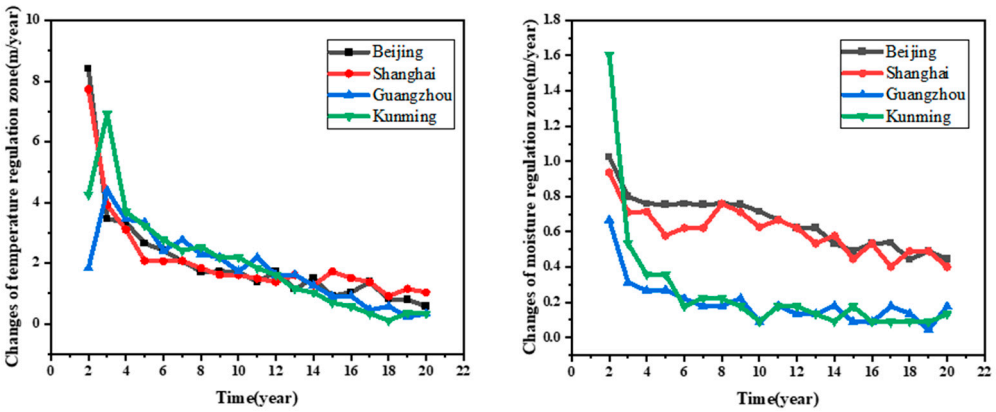


Figure 25. The annual changes in temperature and moisture regulation in four cities: (**a**) temperature regulation zone; (**b**) moisture regulation zone.

5. Conclusions

Based on the coupled heat and moisture transfer of air-surrounding rock in the interval tunnel, Beijing, Shanghai, Guangzhou and Kunming are selected as typical cities in cold region, hot summer and cold winter region, hot summer and warm winter region and mild region respectively. The interannual variations in heat and moisture environments of the metro tunnel in four cities are studied. The main conclusions are as follows:

The air temperature inside tunnels in all four cities exhibits an upward trend over the years, with diminishing annual increments. Over a 20-year period, the maximum air temperatures within the tunnels increased by 1.5 °C, 1.46 °C, 1.3 °C, and 0.98 °C in Beijing, Shanghai, Guangzhou, and Kunming, respectively. Conversely, the relative humidity displays minimal interannual variation, with a noticeable lag effect observed along the tunnel.

The thicknesses of both the temperature regulation zone and the moisture regulation zone within the surrounding rock increase annually. Over two decades, the thicknesses of the temperature regulation zones expanded by 38.85 m, 38.98 m, 34.38 m, and 38.2 m, respectively, while the moisture regulation zones increased by 12.5 m, 12.41 m, 3.78 m, and 4.96 m, respectively.

A comparative analysis of the peak tunnel air temperatures and the corresponding temperature and moisture regulation zones thicknesses indicates that the tunnel air peak temperatures correlate positively with external atmospheric peak temperatures. Furthermore, the annual increase in tunnel air peak temperature intensifies with larger fluctuations in atmospheric temperatures. The disparity between annual mean atmospheric temperature and initial surrounding rock temperature directly influences the thickness of the temperature regulation zone. Additionally, the amplitude of annual atmospheric temperature variation and mean relative humidity significantly impact the moisture regulation zone, with increased atmospheric temperature fluctuations resulting in a thicker regulation zone.

This study primarily investigates the general characteristics of air-surrounding rock heat and moisture exchange within metro tunnels across typical climatic regions in China. This study aims to provide a foundational reference for the evolution of thermal and humid environmental conditions in the surrounding rock of metro tunnel segments, thereby facilitating risk mitigation of potential thermal–humid safety hazards in subway engineering.

For instance, the evolution of the temperature and moisture regulation zones in tunnel surrounding rock across different climate zones can inform the optimization of rock mass protection measures and lining structure designs. Based on the distribution patterns of temperature and humidity of tunnel air, the study also seeks to offer insights into the design and operational strategies of ventilation and dehumidification systems for metro tunnels. Currently, our research findings are insufficient to offer standardized design and construction recommendations validated through practical engineering applications. Future efforts will focus on conducting extensive field investigations and theoretical studies related to the thermal and moisture environment of subway systems. These efforts will progressively enhance the understanding of the heat and moisture behaviors in metro tunnel segments, ultimately aiming to provide effective engineering guidance and recommendations.

There are some limitations in this study. The scope of the study does not cover severe cold regions, and only one representative city is selected from each of the other four climate zones as a research sample, which makes it difficult to fully reflect the differentiated characteristics of different cities in the same climate zone. Further research will further incorporate more diverse climatic and geological backgrounds into the research scope, improve the physical mechanism of the model, and thus more comprehensively reveal the evolution law of the thermal and humid environment of the tunnel.

Author Contributions: Conceptualization, J.M.; methodology, Q.Z.; software, L.H. (Lin Huang); validation, B.D.; formal analysis, L.H. (Lei He); writing—original draft preparation, X.C. and S.Q.; writing—review and editing, J.M., Q.Z. and L.H. (Lei He); supervision, L.H. (Lin Huang) and X.C. All authors have read and agreed to the published version of the manuscript.

Funding: The authors appreciate the financial support from the Research on Thermal and Humid Environment Protection and Flue Gas Control Technology in Deep Space (No.2021KY23ZD(JMRH)-02PT), and the Research on the Development and Design Method of Capillary Energy Wall of Subway Station in Loess Area (No.2023-YBSF-382).

Data Availability Statement: No new data were created or analyzed in this study.

Conflicts of Interest: The authors declare no competing interests. The author Jiangyan Ma, Lin Huang, Baoshun Deng, and Lei He were employed by the company China Railway First Survey and Design Institute Group Co., Ltd. There is no conflict of interest between any of the authors and the company.

Nomenclature

c_v	The specific heat capacity of water vapor, J/(kg·K)
c_w	The specific heat capacity of liquid water, J/(kg·K)
c_s	The specific heat capacity of solid materials, J/(kg·K)
D	The diffusion coefficient, m^2/s
D_w	The diffusion coefficient of liquid water, m^2/s
D_φ	The mass transfer coefficient caused by the relative humidity gradient, kg/(m·s)
D_T	The mass transfer coefficient caused by temperature gradient, $m^2/(s·K)$
G_0	The moisture source, $kg/(m^3·s)$
h	The convective heat transfer coefficient between the tunnel air and the surrounding rock wall, $W/(m^2·K)$
h_m	The convective heat transfer coefficient at the tunnel's surrounding rock surface, s/m
$\vec{J}_l$	The liquid water transfer, $kg/(m^2·s)$
$\vec{J}_v$	The water vapor transfer, $kg/(m^2·s)$
K_l	The permeability of liquid water, kg/(m·s·Pa)
$L(T)$	The latent heat of evaporation, J/kg

P_{sat}	The saturation vapor pressure, Pa
P_v	The vapor pressure, Pa
P_w	The vapor partial pressure at the tunnel's surrounding rock surface, Pa
P_f	The vapor partial pressure of the tunnel air, Pa
q	The heat flow, W/m^2
Q_0	The heat source, W/m^3
R_v	Gas constant of water vapor, $J/(kg{\cdot}K)$
S	The capillary pressure, Pa
T	The temperature, K
T_w	The wall temperature, K
T_f	The air temperature in the tunnel, K
ρ_s	The density of surrounding rock, kg/m^3
ρ_a	The air density, kg/m^3
ρ_w	The density of liquid water, kg/m^3
φ	The relative humidity
δ_v	The water vapor permeability coefficient, $kg/(m{\cdot}s{\cdot}Pa)$
λ	The effective thermal conductivity, $W/(m{\cdot}K)$
λ_{eff}	The effective thermal conductivity of the surrounding rock, $W/(m{\cdot}K)$
v	Airflow velocity, m/s
w	Moisture content, kg/m^3
τ	Time, s

References

1. Cheng, G.H.; Wang, R.; Zhao, M.H.; Su, J.; Yang, Y.; Zhang, X. Current situation and development trend of urban underground space development and utilization in China. *Earth Sci. Front.* **2019**, *26*, 39–47. (In Chinese)
2. Annual Statistics and Analysis Report of Urban Rail Transit 2021. *China Metros* **2022**, 10–15. (In Chinese) [CrossRef]
3. Yu, Y.; You, S.; Zhang, H.; Ye, T.; Wang, Y.; Tang, C.; Wei, S. Measuring and modeling moisture environment in underground metro stations during commissioning stage: A case study. *Build. Serv. Eng. Res. Technol.* **2022**, *43*, 241–259. [CrossRef]
4. Wang, J.; Feng, X.; Zeng, X.; Chen, J.; Shi, T.; Zhang, G.; Liao, J. Research on the effectiveness of ventilation and dehumidifier on preventing condensation risk of urban utility tunnel. *Int. J. Vent.* **2025**, *24*, 277–291. [CrossRef]
5. Song, H.; Li, J.; Yu, Y.; Chen, Q. Research on the Influence of Subway Tunnel Depth on Heat Storage Characteristics of the Surrounding Soil Mass. *Appl. Sci.* **2023**, *13*, 9534. [CrossRef]
6. Tong, L.; Zhang, M.; Hu, S.; Ji, Y. Changing Rules in Subway Tunnel Thermal Environment and Comprehensive Utilization of Waste Heat. *Buildings* **2024**, *14*, 2524. [CrossRef]
7. Ji, Y.; Wang, W.; Fan, Y.; Hu, S. Coupling Effect between Tunnel Lining Heat Exchanger and Subway Thermal Environment. *Renew. Energy* **2023**, *217*, 119165. [CrossRef]
8. Zhu, S.; Cheng, J.; Song, W.; Borowski, M.; Zhang, Y.; Yu, B.; Wang, Y.; Qi, C.; Tukkaraja, P.; Hua, G.; et al. Using seasonal temperature difference in underground surrounding rocks to cooling ventilation airflow: A conceptual model and simulation study. *Energy Sci. Eng.* **2020**, *8*, 3457–3475. [CrossRef]
9. Wang, L.; Zou, X.; Tao, H.; Song, J.; Zheng, Y. Experimental Study on Evolution Characteristics of the Heat Storage of Surrounding Soil in Subway Tunnels. *Procedia Eng.* **2017**, *205*, 2728–2735. [CrossRef]
10. Wang, M.; Geng, M.; Liu, L.; Wang, Y.; Shang, S. Numerical and Experimental Study on the Cooling Performance of Cold Load Storage Functional Backfill Considering the Coupled Heat and Moisture Transfer. *J. Build. Eng.* **2023**, *78*, 107673. [CrossRef]
11. Li, Z.; Xu, Y.; Li, R.; Jia, M.; Wang, Q.; Chen, Y. Impact of the Water Evaporation on the Heat and Moisture Transfer in a High-Temperature Underground Roadway. *Case Stud. Therm. Eng.* **2021**, *28*, 101551. [CrossRef]
12. Liu, N.; Liang, S.; Wang, S.; Song, Z. THM model of rock tunnels in cold regions and numerical simulation. *Sci. Rep.* **2024**, *14*, 3465. [CrossRef]
13. Jiang, H.; Niu, F.; Ma, Q.; Su, W.; Wang, E. Numerical Analysis of Heat Transfer between Air inside and Outside the Tunnel Caused by Piston Action. *Int. J. Therm. Sci.* **2021**, *170*, 107164. [CrossRef]
14. Vasilyev, G.P.; Peskov, N.V.; Lysak, T.M. Heat Balance Model for Long-Term Prediction of the Average Temperature in a Subway Tunnel and Surrounding Soil. *Int. J. Therm. Sci.* **2022**, *172*, 107344. [CrossRef]
15. Sun, T.; Luo, Z.; Chay, T. An Analytical Model to Predict the Temperature in Subway-Tunnels by Coupling Thermal Mass and Ventilation. *J. Build. Eng.* **2021**, *44*, 102564. [CrossRef]
16. De Vries, D.A. Simultaneous Transfer of Heat and Moisture in Porous Media. *Eos Trans. Am. Geophys. Union* **1958**, *39*, 909–916.

17. Philip, J.R. Evaporation, and Moisture and Heat Fields in the Soil. *J. Meteorol.* **1957**, *14*, 354–366. [CrossRef]
18. Vries, D.; Daniel, A. The Theory of Heat and Moisture Transfer in Porous Media Revisited. *Int. J. Heat Mass Transf.* **1987**, *30*, 1343–1350. [CrossRef]
19. Philip, J.R.; De Vries, D.A. Moisture Movement in Porous Materials under Temperature Gradients. *Eos Trans. Am. Geophys. Union* **1957**, *38*, 222–232.
20. Lykov, A.V. On Systems of Differential Equations for Heat and Mass Transfer in Capillary Porous Bodies. *J. Eng. Phys.* **1974**, *26*, 11–17. [CrossRef]
21. Luikov, A.V. Heat and Mass Transfer in Capillary-Porous Bodies. *Adv. Heat Transf.* **1964**, *1*, 123–184.
22. Yang, Z. Study on the Influence of Line Connectivity on Subway Piston Wind and Air Temperature. Master's Thesis, Southwest Jiaotong University, Chengdu, China, 2021. (In Chinese)
23. *GB 50038-2005*; Code for Design of Civil Air Defense Basement. China Plan Publishing House: Beijing, China, 2005. (In Chinese)
24. Gao, X.; Qu, Y.; Xiao, Y. A Numerical Method for Cooling and Dehumidifying Process of Air Flowing through a Deeply Buried Underground Tunnel with Unsaturated Condensation Model. *Appl. Therm. Eng.* **2019**, *159*, 113891. [CrossRef]
25. Zhi, T.; Ning, K. Humidity Migration in Building Structures. *Adv. Mech.* **1994**, *24*, 441–458. (In Chinese)
26. Pedersen, C.R. Prediction of Moisture Transfer in Building Constructions. *Build. Environ.* **1992**, *27*, 387–397. [CrossRef]
27. *EN 15026:2007*; Hygrothermal Performance of Building Components and Building Elements-Assessment of Moisture Transfer by Numerical Simulation. National Standards Authority of Ireland: Dublin, Ireland, 2007.
28. Wei, M.; Wang, B.; Liu, S. Simulation of Thermo-Humid Coupled Transfer in Deep-Buried Underground Engineering Enclosures Using COMSOL Multiphysics. *Sci. Technol. Eng.* **2020**, *20*, 5729–5736. (In Chinese)
29. Wang, L. Subway Piston Wind and Subway Environmental Control Energy Saving. Ph.D. Thesis, Tongji University, Shanghai, China, 2007. (In Chinese)
30. Zhou, X.; Cao, X.; Leng, Z.; Zeng, C.; Yuan, Y.; Attia, S. Hygrothermal behavior of energy diaphragm wall and the induced heat and moisture interaction with adjacent underground space. *Undergr. Space* **2025**, *23*, 193–219. [CrossRef]
31. Li, R. *Basic of Finite Volume Method*; National Defense Industry Press: Beijing, China, 2008. (In Chinese)
32. van Schijndel, A.W.M.; Goesten, S.; Schellen, H.L. Simulating the Complete Hamstad Benchmark Using a Single Model Implemented in Comsol. *Energy Procedia* **2017**, *132*, 429–434. [CrossRef]

Disclaimer/Publisher's Note: The statements, opinions and data contained in all publications are solely those of the individual author(s) and contributor(s) and not of MDPI and/or the editor(s). MDPI and/or the editor(s) disclaim responsibility for any injury to people or property resulting from any ideas, methods, instructions or products referred to in the content.